nature chemistry

ARTICLES

https://doi.org/10.1038/s41557-019-0351-5

Expedited mapping of the ligandable proteome using fully functionalized enantiomeric probe pairs

Yujia Wang[1], Melissa M. Dix[1], Giulia Bianco[2], Jarrett R. Remsberg[1], Hsin-Yu Lee[1], Marian Kalocsay[3], Steven P. Gygi[3], Stefano Forli[2], Gregory Vite[4], R. Michael Lawrence[4], Christopher G. Parker[1,5]* and Benjamin F. Cravatt[1]*

A fundamental challenge in chemical biology and medicine is to understand and expand the fraction of the human proteome that can be targeted by small molecules. We recently described a strategy that integrates fragment-based ligand discovery with chemical proteomics to furnish global portraits of reversible small-molecule/protein interactions in human cells. Excavating clear structure–activity relationships from these 'ligandability' maps, however, was confounded by the distinct physicochemical properties and corresponding overall protein-binding potential of individual fragments. Here, we describe a compelling solution to this problem by introducing a next-generation set of fully functionalized fragments differing only in absolute stereochemistry. Using these enantiomeric probe pairs, or 'enantioprobes', we identify numerous stereoselective protein–fragment interactions in cells and show that these interactions occur at functional sites on proteins from diverse classes. Our findings thus indicate that incorporating chirality into fully functionalized fragment libraries provides a robust and streamlined method to discover ligandable proteins in cells.

Chemical probes are versatile tools to interrogate the functions of proteins in biological systems and complement genetic approaches[1] by producing reversible and graded gains or losses of protein activity, as well as, in certain instances, neo-functional outcomes[2–5]. Small molecules also represent a principal category of clinically approved drugs, and quality chemical probes are needed to pharmacologically characterize novel targets on the path to developing therapeutic agents.

Despite their basic and translational value, chemical probes are lacking for the vast majority of human proteins[6]. Methods for the discovery of new chemical probes often rely on high-throughput screening (HTS) of large libraries (~10^6) of relatively high molecular weight and structurally diverse compounds against individual proteins (target-based) or cellular systems (phenotype-based)[7,8]. Hits from such libraries can often be challenging to optimize due to their structural complexity and suboptimal ligand efficiencies[9]. Further, many proteins are problematic to express, purify and format for in vitro HTS, especially if they are parts of large complexes and/or remain poorly characterized in terms of biochemical function. These challenges underscore the need for new methods that can more broadly assess the 'ligandability' (that is, ability to bind small molecules) of the human proteome in native biological systems.

Fragment-based ligand discovery (FBLD) has emerged as a versatile approach for the discovery of atom-efficient, small-molecule binders for a wide range of proteins[10–12]. However, due to the generally low affinity of fragment hits and the biophysical methods typically used for their discovery (for example, NMR, surface plasmon resonance, isothermal calorimetry), FBLD has been limited mostly to the study of purified proteins in vitro[11]. We recently introduced a strategy that integrates FBLD with chemical proteomics to globally assess small-molecule/protein interactions in human cells[13]. Using a specialized library of fully functionalized fragment (FFF) probes, which possess variable fragment binding elements coupled to photoreactive and bioorthogonal reporter groups, we mapped >2,000 reversible fragment–protein interactions in human cells and showed that these discoveries can be advanced to create more potent and selective compounds capable of modulating the activity of proteins in cells[13].

The fragment binding elements in our initial studies were selected based on their representation in drug-like molecules[14] and were accordingly diverse in structure and physicochemical properties. As a consequence, we found that individual FFF probes showed substantial differences in their overall proteomic interaction profiles, which made for complicated structure-activity relationships (SARs) requiring careful manual review to identify fragment–protein interactions that reflected authentic recognition events (versus simply correlating with the overall proteomic interaction profiles of the FFF probes). We describe herein a general strategy to address this confounding bottleneck in the form of a next-generation set of FFF probes consisting of physicochemically matched fragment pairs differing only in absolute stereochemistry. The stereoselective engagement of protein targets is a feature of numerous chemical probes and drugs[15–19] and we reasoned that this outcome, measured on a proteome-wide scale, would provide instant evidence of specific interactions between small-molecule fragments and proteins in cells. Using a set of eight pairs of enantiomeric FFF probes—or 'enantioprobes'—we expeditiously identify >170 stereochemistry-dependent small-molecule/protein interactions in human cells.

[1]Department of Chemistry, The Scripps Research Institute, La Jolla, CA, USA. [2]Department of Integrative Structural and Computational Biology, The Scripps Research Institute, La Jolla, CA, USA. [3]Department of Cell Biology, Harvard Medical School, Boston, MA, USA. [4]Research and Development, Bristol-Myers Squibb Company, Princeton, NJ, USA. [5]Department of Chemistry, The Scripps Research Institute, Jupiter, FL, USA.
*e-mail: cparker@scripps.edu; cravatt@scripps.edu

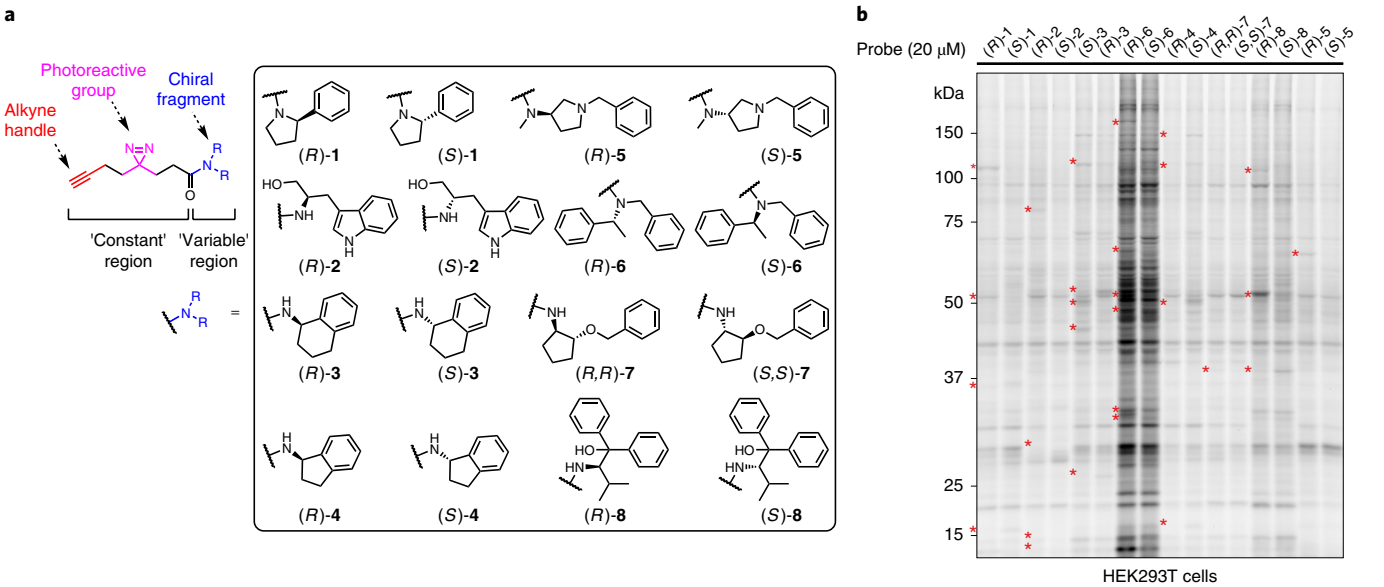

Fig. 1 | Enantioprobes for mapping stereoselective protein–small molecule fragment interactions in human cells. a, Structures of enantioprobes, which consist of a 'variable' element of stereopure fragment pairs (enclosed box) and a 'constant' region containing a diazirine photoreactive group and a clickable alkyne handle. **b**, Gel-based profiling of enantioprobe–protein interactions in human cells. HEK293T cells were treated with enantioprobes (20 μM) for 30 min, photocrosslinked and lysed, and proteomes were conjugated to an azide-rhodamine tag using CuAAC chemistry and analysed by SDS–PAGE and in-gel fluorescent scanning. Red asterisks mark representative stereoselective enantioprobe–protein interactions. The gel image reflects representative results from two independently performed experiments.

The enantioprobe targets span diverse structural and functional classes and include proteins that lack chemical probes. We confirm enantioprobe interactions for several recombinantly expressed proteins and show that the interactions occur at functionally relevant sites on these proteins. Finally, we describe a quantitative, multiplexed workflow capable of performing up to five enantioprobe pair comparisons in a single experiment, thereby greatly increasing the throughput and dimensionality of fragment-based ligand discovery in cells.

Results

Design and initial proteomic profiling of enantioprobes. The FFF probes in our original set were designed to contain the following: (1) a 'variable' recognition element consisting of structurally diverse small-molecule fragments intended to promote interactions with distinct proteins in human cells; and (2) a structurally minimized 'constant' region bearing a photoactivatable diazirine group and alkyne handle, which together enabled UV-light-induced covalent modification and detection, enrichment, and identification of fragment-interacting protein targets (Fig. 1a)[13]. We reasoned that the introduction of stereochemistry into FFF probe design could furnish pairs of compounds that display equivalent physicochemical properties and gross overall protein binding in cells, but differ in their stereoselective interactions with authentic binding pockets for small molecules in certain proteins. The preferential enrichment of a protein by one member of an enantioprobe pair would thereby constitute instant evidence of ligandability for that protein.

We synthesized a library of eight enantioprobe pairs, where members of each pair differ only in absolute stereochemistry of the fragment recognition element (Fig. 1a). We then qualitatively assessed the overall proteomic interaction profiles for the enantioprobes using established SDS–polyacrylamide gel electrophoresis (SDS–PAGE) methods[13]. In brief, we treated HEK293T cells with each enantioprobe (20 μM, 30 min) followed by exposure to UV light (365 nm, 10 min), harvesting, lysis, coupling of probe-modified proteins to an azide-rhodamine reporter tag using copper-catalysed azide-alkyne cycloaddition chemistry (CuAAC)[20] and visualization of these proteins by SDS–PAGE and in-gel fluorescence scanning. As expected, we observed substantial differences in protein interactions across the enantioprobe pairs, with one probe pair ((*R*) and (***S***)-**6**) exhibiting much greater overall protein labelling compared to others (Fig. 1b). Encouragingly, however, the (*R*) and (*S*) members within each enantioprobe pair showed similar overall proteomic labelling with the exception of select proteins that exhibited stereochemistry-dependent ('stereoselective') interactions (Fig. 1b and Supplementary Fig. 1, red asterisks). The enantioprobe pairs also showed clear increases in protein labelling across a test concentration range of 5–100 μM (Supplementary Fig. 1), indicating good cell permeability, and virtually all of these protein labelling events were dependent on UV light exposure (Supplementary Fig. 1). We next turned our attention to mapping enantioprobe–protein interactions in human cells by quantitative mass spectrometry (MS)-based proteomics.

Global maps of enantioprobe–protein interactions in human cells. We evaluated two complementary cell types for enantioprobe interactions by quantitative MS-based proteomics: (1) primary human peripheral blood mononuclear cells (PBMCs); and (2) HEK239T cells. The selection of these cell types afforded an opportunity to directly compare enantioprobe profiles to those generated with the original set of FFF probes (generated in HEK293T cells)[13] and extend our understanding of fragment ligandability to primary human immune cells. Both cell types were treated with equal concentrations of (*R*)- or (*S*)-compounds from each enantioprobe pair (200 μM, 30 min) and then exposed to UV light to induce photocrosslinking of enantioprobe-bound proteins. Cells were lysed, and the enantioprobe-labeled proteins were conjugated to an azide-biotin tag by CuAAC chemistry, enriched by streptavidin and analysed by MS-based proteomics, where stereoselective interactions were quantified by isotopic labelling using either reductive dimethylation (ReDiMe) with heavy or light formaldehyde (PBMCs)[21,22] or SILAC (stable isotope labelling by amino acids in cell culture; HEK293T

cells)[23] (Fig. 2a). For PBMCs, these experiments were performed in replicate in both isotopic directions (heavy vs light and light vs heavy) to furnish four independent experiments for each enantioprobe pair, and, for HEK293T cells, a subset of the enantioprobe pairs was similarly examined. We operationally defined a protein as engaging in a 'stereoselective' interaction if it showed preferential enrichment by an average value of >2.5-fold by one member of an enantioprobe pair in either PBMCs or HEK293T cells. For the SILAC studies in HEK293T cells, we also performed control experiments where the heavy- and light-labeled cells were treated with the same enantioprobe to ensure that, under these conditions, enantioprobe-enriched proteins showed a ratio of ~1.0. (Supplementary Fig. 2, Supplementary Dataset 1 and Supplementary Dataset 2).

In total, 176 proteins showed stereoselective interactions with one or more enantioprobe pairs, which included 119 proteins identified in PBMCs (Fig. 2b, Supplementary Dataset 1 and Supplementary Dataset 2) and 108 proteins identified in HEK293T cells (Supplementary Fig. 2, Supplementary Dataset 1 and Supplementary Dataset 2). We observed similar numbers of stereoselective protein interactions for each member of an enantioprobe pair (Fig. 2c and Supplementary Fig. 2), indicating equivalent potential for the *R* or *S* enantiomer to preferentially enrich proteins. Proteins identified in both PBMCs and HEK293T cells generally showed consistent profiles across the cell types; that is, stereoselective interactions identified in PBMCs were also observed in HEK293Ts and vice versa (Fig. 2d and Supplementary Fig. 2). The enantioprobe pairs displayed considerable differences in their total number of stereoselective interactions with the human proteome (Fig. 2e), and, notably, these profiles were unrelated to the extent of overall protein labelling displayed by the probes (Fig. 1b). This result suggests that stereoselective interactions are based on factors beyond the general protein binding potential of a given fragment structure.

The majority of proteins showing stereoselective interactions (>80%) did so with only one of the enantioprobe pairs (Fig. 2f and Supplementary Fig. 2). Embedded within this specificity were multiple profiles, including proteins that were enriched by several enantioprobe pairs but stereoselectively by one pair, as well as proteins that showed strong enrichment predominantly with a single enantioprobe across the entire probe set (Fig. 2g). Proteins showing stereoselective interactions with enantioprobes spanned diverse functional and structural classes (Fig. 3a, Supplementary Table 1 and Supplementary Dataset 1). Perhaps unsurprisingly, many of the enantioprobe targets were enzymes, including kinases, methyltransferases and various metabolic enzymes (Fig. 3a, Supplementary Table 1 and Supplementary Dataset 1), likely reflecting the high potential for these proteins to specifically bind small molecules. We also, however, observed stereoselective interactions for various scaffolding/adaptor proteins and transcriptional regulators—classes that have been historically considered challenging to target with small molecules (Fig. 3a, Supplementary Table 1 and Supplementary Dataset 1). To the extent that the magnitude of stereoselective enrichment is predictive of a robust small-molecule interaction, we further noted that high stereoselective enrichment (ratio values >4.0 in pairwise comparisons of *R* vs *S* enantioprobes) was observed for several scaffolding/adaptor proteins and transcriptional regulators (Supplementary Table 1 and Supplementary Dataset 1). Enantioprobe targets that were observed in PBMCs, but not in HEK293T cells, tended to correspond to immune-enriched proteins (for example, IRAK3 (ref. [24]), PARP10 (ref. [25])) (Supplementary Dataset 1). Finally, we observed limited overlap of enantioprobe targets with proteins that demonstrated ligandability in previous chemical proteomic studies using cysteine-[26,27] or lysine-reactive[28] electrophilic fragments (Fig. 3b), indicating that non-covalent and covalent fragments generally interact with distinct sets of proteins in human cells. Moreover, while many of the enantioprobe targets were also enriched by members of the original FFF probe set[13], these previous profiles often did not provide useful SAR information, either reflecting substantial enrichment by all of the FFF probes or mirroring the respective global protein interaction footprints of these probes (Supplementary Fig. 2).

Enantioprobes engage functionally relevant sites on proteins. We next sought to confirm stereoselective interactions for representative proteins targeted by diverse enantioprobes and originating from different functional classes, including enzymes (kinase, RPS6KA3; methyltransferase, SMYD3; and a metabolic enzyme, DCTPP1), a lipid-binding protein (UNC119B), a transporter (TSPO), a membrane-binding/adaptor protein (PACSIN2), a transcriptional regulator (HDGF) and an uncharacterized protein (TTC38). Each protein was recombinantly expressed with a FLAG epitope tag in HEK293T cells by transient transfection, and 48 h later, cells were treated with the indicated enantioprobe pair (5–80 μM, unless otherwise indicated) followed by photocrosslinking with UV light, CuAAC coupling to an azide-rhodamine tag and visualization of protein labelling by SDS–PAGE and in-gel fluorescence scanning. All experiments also included mock-transfected cells as a control. Each recombinantly expressed protein displayed stereoselective interactions with the enantioprobes that mirrored the preferential labelling of the endogenous forms of these proteins in PBMCs or HEK293T cells (Fig. 3c–f and Supplementary Fig. 3). Most of these stereoselective interactions could be detected with 5–10 μM of the preferred enantioprobe and were preserved across the entire enantioprobe concentration range (Fig. 3c–f and Supplementary Fig. 3).

Some of the protein targets have known ligands, which afforded an opportunity to test whether the enantioprobes and ligands share a common binding site on these proteins. Four representative proteins were selected for analysis: (1) the lysine methyltransferase SMYD3, a target of **(*R*)-1** and **(*R*)-5** that binds both cofactors (SAM, SAH) and the inhibitor **EPZ031686**[29,30]; (2) the lipid-binding protein UNC119B, a target of **(*R*)-1** and **(*R*)-5** that binds the natural product **squarunkin A**[31]; (3) the sterol transporter TSPO, a target of **(*R,R*)-7** that binds the ligand PK 11195[32,33], which is used to image brain injury and inflammation[34,35]; and (4) the uncharacterized protein TTC38, a target of **(*S*)-4** that has been found to bind the histone deacetylase inhibitor panobinostat[36]. In all four cases, we found that enantioprobe interactions with both the endogenous and recombinantly expressed protein targets were competitively blocked by increasing concentrations of ligand, as measured by MS-based (endogenous protein) and gel-based (recombinant protein) methods (Fig. 4a,b and Supplementary Fig. 4). We further assessed the relative magnitude of target enrichment and competition measured with pure enantioprobes versus racemic mixtures of these probes. As expected, racemic mixtures of enantioprobes show substantially reduced enrichment of stereoselective protein targets compared to the preferred enantioprobes (Supplementary Fig. 4). More interestingly, however, these experiments also uncovered qualitative differences in how individual protein targets interact with enantioprobes. We found, for instance, that the inhibitor **EPZ031686** blocked the labelling of SMYD3 by the preferred enantioprobe **(*R*)-1**, but not the non-preferred enantioprobe **(*S*)-1** (Supplementary Fig. 4). In contrast, **squarunkin A** blocked the interaction of UNC119B with both the preferred and non-preferred enantioprobes (**(*R*)-1** and **(*S*)-1**, respectively; Supplementary Fig. 4). These data indicate that, for some protein targets (for example, UNC119B), the magnitude of observed stereoselectivity reflects a difference in specific interactions with both enantioprobes, while for other proteins (for example, SMYD3), the degree of stereoselectivity may be even greater than that experimentally measured, potentially being suppressed by low-level nonspecific interactions with the non-preferred enantioprobe.

For SMYD3, only **EPZ031686**, but not SAM or SAH, blocked **(*R*)-1** interactions (Fig. 4a). Structural studies have shown that

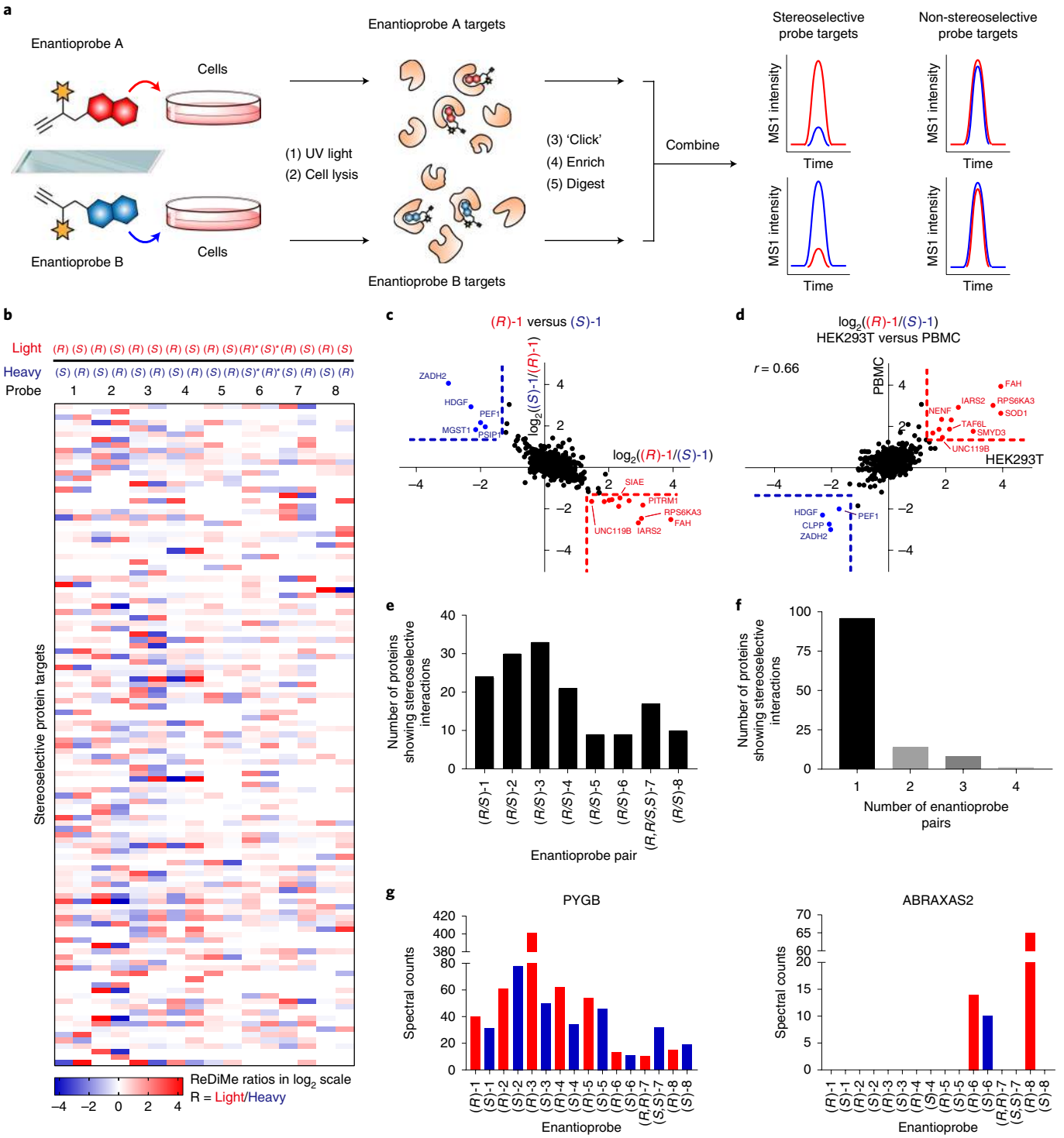

Fig. 2 | MS-based profiling of enantioprobe–protein interactions in human cells. a, Schematic workflow for identifying stereoselective enantioprobe–protein interactions in human cells. **b**, Heatmap showing relative protein enrichment ratios for pairwise comparisons of (*R*) and (*S*) enantioprobes (200 μM each) in both isotopic directions in human PBMCs. White signals in the heatmap correspond to either proteins with ratio values of ~1 or proteins that were not enriched and quantified with the indicated enantioprobe pair. (*R*)* and (*S*)* represent (*R,R*) and (*S,S*) for enantioprobe **7**. **c**, Representative scatter plot showing protein enrichment ratios for **(*R*)-1** versus **(*S*)-1** in PBMCs. Proteins enriched >2.5-fold by one enantiomer over the other are considered stereoselective targets. Red and blue protein targets show stereoselective interactions with **(*R*)-1** and **(*S*)-1**, respectively. Data reflect an average of at least two independently performed experiments for each isotopic direction that provided similar results (see Supplementary Dataset 2). **d**, Similar stereoselective interactions are observed in different cell types. Plot depicts $\log_2$ values of protein enrichment ratios for **(*R*)-1**/**(*S*)-1** in HEK293T cells (*x*-axis) versus PBMCs (*y*-axis). The graph contains 812 total quantified proteins. *r* values are Pearson correlation coefficients. Data reflect an average of two independently performed experiments that provided similar results (see Supplementary Dataset 2). **e**, Number of stereoselective protein interactions found for each enantioprobe pair in PBMCs. **f**, Number of proteins showing stereoselective interactions with the indicated number of enantioprobe pairs in PBMCs. **g**, Quantity of aggregate spectral counts for PYGB (left graph) and ABRAXAS2 (right graph) enriched by each enantioprobe in PBMCs.

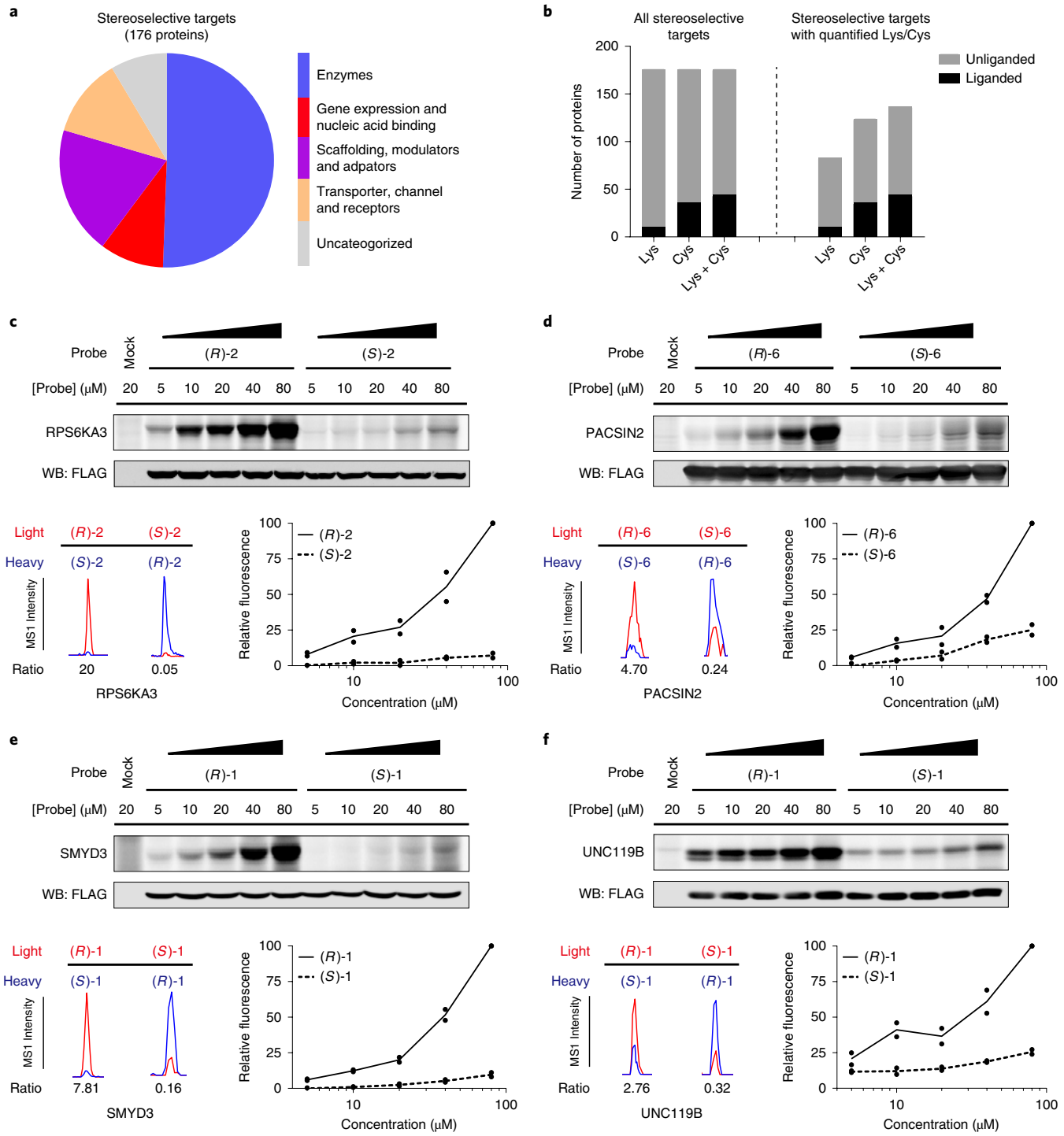

Fig. 3 | Characterization of stereoselective protein targets of enantioprobes. a, Functional classes of stereoselective protein targets of enantioprobes in PBMCs and HEK293T cells. **b**, Fraction of stereoselective protein targets of enantioprobes showing evidence of ligandability with cysteine- and/or lysine-reactive fragments, as determined previously[26–28]. The left graph includes all stereoselective targets; the right graph shows only those stereoselective targets with quantified cysteines and/or lysines in previous studies[26–28]. **c–f**, Top: confirmation of stereoselective enantioprobe–protein interactions with recombinantly expressed proteins. RPS6KA3 (**c**), PACSIN2 (**d**), SMYD3 (**e**) and UNC119B (**f**) were recombinantly expressed with FLAG epitope tags by transient transfection in HEK293T cells, and transfected cells were then treated with the indicated concentrations of enantioprobes, photocrosslinked and lysed, and proteomes were conjugated to an azide-rhodamine tag by CuAAC chemistry and analysed by SDS–PAGE and in-gel fluorescence scanning. Gel images reflect representative results from two independently performed experiments. Bottom left: extracted MS1 chromatograms of representative tryptic peptides for endogenous forms of the protein targets in HEK293T cells or PBMCs treated with indicated enantioprobes (200 μM). Bottom right: quantification of protein labelling by the indicated enantioprobes derived from gel-based profiles shown in top section. Data reflect two independently performed experiments. Confirmation of additional stereoselective interactions shown in Supplementary Fig 3.

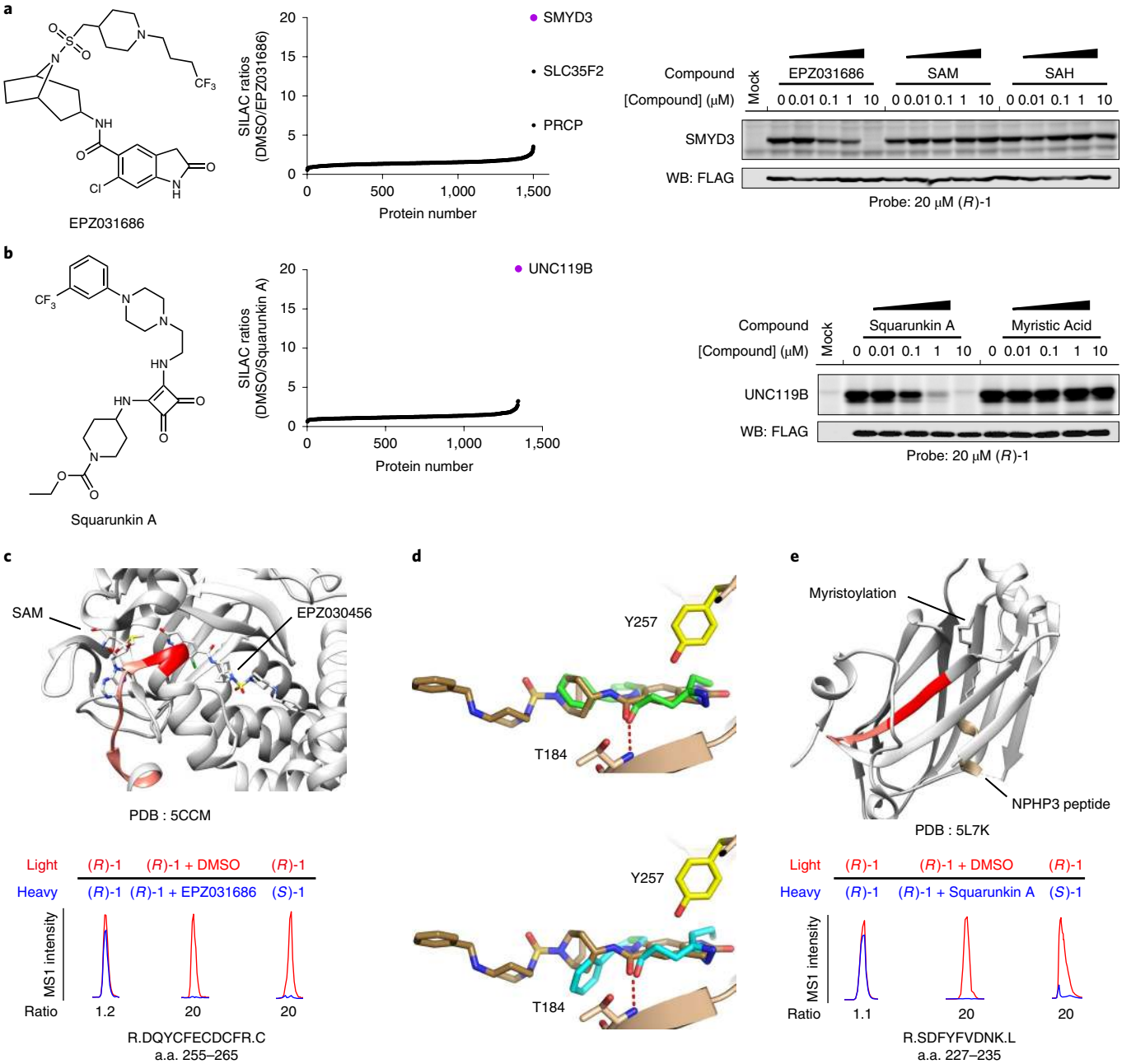

Fig. 4 | Stereoselective interactions occur at functional and druggable sites on protein targets of enantioprobes. a,**b**, Left: structure of competitor ligands; **EPZ031686** (**a**); **squarunkin A** (**b**). Middle: waterfall plots of competitive blockade of enantioprobe (200 μM) interactions with endogenous protein targets for corresponding ligands (20 μM) in HEK293T cells. Data reflect average values from two independently performed experiments that provided similar results (see Supplementary Dataset 2). Right: gel-based profiles of competitive blockade of enantioprobe interactions with recombinantly expressed protein targets for corresponding ligands in transfected HEK293T cells. Gel images reflect representative results from two independently performed experiments. **c**, Structure of SMYD3 in complex with EPZ030456 (shown as stick model; PDB 5CCM) highlighting tryptic peptide modified with ***(R)*-1** (a.a. 255–265, light red; predicted probe-modified residues D255–Y257, dark red). **d**, Predicted binding modes of enantioprobe ***(R)*-1** (top, green sticks) or ***(S)*-1** (bottom, cyan sticks) to SMYD3, as determined by docking simulations, superimposed on the co-crystallized complex of EPZ030456 inhibitor and SMYD3 (brown sticks). Predicted hydrogen bonds between ***(R)*-1** or ***(S)*-1** and T184 of SMYD3 are depicted as red dashed lines. **e**, Structure of UNC119A in complex with a myristoylated peptide from NPHP3 (yellow; PDB 5L7K) highlighting tryptic peptide modified with ***(R)*-1** (a.a. 227–235, light red, predicted probe-modified residues S227–Y230, dark red).

EPZ031686 binds in the lysine substrate binding pocket of SMYD3 and noncompetitively with SAM[29]. These data suggested that (***R*)-1** may also bind to the lysine substrate pocket, which we confirmed by mapping the site of (***R*)-1** photolabelling on SMYD3 by quantitative MS. Using previously described protocols[13,37,38], we identified a single tryptic peptide in SMYD3 that was photolabeled by (***R*)-1**—R.DQYCFECDCFR.C (amino acids (a.a.) 255–265)—with the predicted site(s) of photoreactivity being residues D255–Y257. These residues are located within 3.6 Å of an **EPZ031686** analogue in the SMYD3 co-crystal structure (Fig. 4c), and Y257 specifically has been found to interact with the methylated lysine in substrate co-crystal structures[39]. Quantitative MS-based proteomics further

demonstrated that photolabelling of the a.a. 255–265 peptide by **(*R*)-1** was blocked by co-incubation with **EPZ031686** and was not observed with the inactive enantioprobe **(*S*)-1** (Fig. 4c). To better understand the molecular basis for the stereoselective interaction of **(*R*)-1** with SMYD3, we performed conventional docking simulations, which revealed that, when binding freely to SMYD3, **(*R*)-1** can adopt two major energetically equivalent poses that would engage the SMYD3 pocket in different ways—one placing the diazirine 4.5 Å from the amide of Q256, and the other positioning the diazirine 3.1 Å from the Oη of Y257 (Supplementary Fig. 4). The latter binding mode, in addition to placing the diazirine closer to the mapped region of **(*R*)-1** labelling of SMYD3, also matched more closely the molecular envelope of other co-crystallized SMYD3 inhibitors (for example, EPZ030456, PDB 5CCM; an oxindole screening hit, PDB 5CCL), with the **(*R*)-1** amide overlapping with the inhibitor amide and hydrogen bonding with T184, and the **(*R*)-1** aromatic ring overlapping with the azabicyclic ring of EPZ030456 to engage a hydrophobic region (Fig. 4d, top).

The docking results also helped to explain the stereoselectivity of the **(*R*)-1**-SMYD3 interaction, as, while **(*S*)-1** was able to reproduce a similar binding mode, the inverted chiral centre reduced the quality of the docking match by placing the hydrophobic phenyl ring outside the molecular envelope of the inhibitor EPZ030456 and towards the hydrophilic side chains T184 and E192 (Fig. 4d, bottom). Finally, to further support these conventional docking results, we also performed covalent docking studies, where we simulated the conformational rearrangements occurring when the **(*R*)-1** diazirine reacts with the Y257 side chain of SMYD3. These covalent docking experiments predicted that minimal molecular rearrangements would be required to accommodate a reaction between **(*R*)-1** and the Oη of Y257 of SMYD3 (Supplementary Fig. 4). Taken together, these molecular modelling findings suggest that the stereoselective interaction between **(*R*)-1** and SMYD3 reflects a preferred binding mode for this chemical probe over the enantiomer **(*S*)-1**.

We also mapped the primary sites of enantioprobe labelling for UNC119B (Fig. 4e) and TSPO (Supplementary Fig. 4) and confirmed the stereoselectivity of these labelling events and their blockade by treatment with competitive ligands (**squarunkin A** and PK 11195, respectively). For UNC119B, **(*R*)-1** modified the tryptic peptide containing residues 227–236 (R.SDSFYFVDNK.L) with predicted sites of labelling spanning S227–Y231 (Fig. 4e). These residues represent a highly conserved stretch of amino acids in UNC119 proteins that are within 2.5 Å of a fatty acylated peptide in a co-crystal structure with the related protein UNC119A[40], and S229 is predicted to hydrogen bond with **squarunkin A** in a docking model of the natural product bound to UNC119A[31] (Fig. 4e). For TSPO, **(*R,R*)-7** modified the *N*-terminal peptide (a.a. 2–24, M.APPWVPAMGFTLAPSLGCFVGSR.F) with the principle site of labelling being C19 (Supplementary Fig. 4). In the solution structure of mouse TSPO, the corresponding residue (G19) is 2.8 Å away from the ligand PK 11195[32].

Taken together, our follow-up studies on representative targets indicate that enantioprobes engage functionally relevant and druggable sites on diverse classes of proteins. We also noted that our chemical proteomic studies with enantioprobes identified additional, unanticipated targets for some of the tested small-molecule competitors. For instance, **EPZ031686** blocked **(*R*)-1** interactions with the solute carrier SLC35F2 and the peptidase PRCP (Fig. 4a), while PK 11195 decreased **(*R,R*)-7** interactions with the lipid-binding protein ABHD5 (Supplementary Fig. 4). While ABHD5 also showed independent evidence of stereoselective interactions with enantioprobes (Supplementary Dataset 1), SLC35F2 and PRCP did not (Supplementary Dataset 1), suggesting that these latter proteins may specifically bind enantioprobes, but without stereochemical preference. Motivated to explore this general concept further, as well as to increase the throughput of and information provided by our chemical proteomic experiments, we set out to create a multiplexed platform for the streamlined analysis of enantioprobe–protein interactions in human cells.

Multiplexed analysis of enantioprobe–protein interactions in cells. While we were generally satisfied with the sensitivity and robustness of our chemical proteomic experiments using SILAC or ReDiMe as quantitative MS-based measurement protocols of enantioprobe–protein interactions, we also recognized that the pairwise nature of these comparisons had drawbacks. Prominently, the limited throughput prevented a deeper exploration of SARs both within and across enantioprobe pairs. For instance, a protein that interacts specifically, but without stereo-preference, with both enantioprobes in a pairwise comparison is difficult to distinguish from a non-specific interaction, as both outcomes furnish an enrichment ratio of ~1.0. And, relatedly, the stochastic nature of protein identification events in untargeted MS-based proteomic experiments hinders confident assignment of proteins that selectively interact with one or a subset of enantioprobes across different experiments. Finally, the throughput of pairwise comparisons also becomes restrictive when attempting to compare the protein interaction profiles of several enantioprobes under various conditions (for example, different cell types or probe concentrations).

We considered that many of the aforementioned challenges could be addressed by analysing enantioprobes with a multiplexed approach for quantitative MS-based proteomics that uses isobaric tandem mass tags (TMTs)[41–43]. In this workflow, up to 10 separate populations of cells are each treated with an enantioprobe (200 μM, 30 min), photocrosslinked, lysed, conjugated to biotin azide via CuAAC, enriched and trypsinized as described above. Tryptic peptides stemming from each treatment group are then labeled with a TMT of equivalent parent mass, but differentiable by MS3-derived fragmentation products, combined, and analysed in a single MS experiment (Fig. 5a) [43]. Applying 10-plex TMTs, we compared the protein interaction profiles of four enantioprobe pairs (Supplementary Dataset 3), alongside a previously described methyl control probe[13] (in duplicate), in human PBMCs and HEK293T cells (Fig. 5b and Supplementary Fig. 5). We required that at least three unique peptides were quantified for each protein to interpret stereoselective interactions with enantioprobes, and stereoselective interactions were defined as those displaying >2.5-fold differential enrichment between (*R*) and (*S*) members of at least one enantioprobe pair, along with >5-fold enrichment over the methyl control probe.

We observed a robust overall correlation between the enantioprobe profiles quantified by multiplexed (TMT-based) versus pairwise (ReDiMe/SILAC) comparative proteomic experiments (Fig. 5c,d and Supplementary Fig. 5), and the vast majority (>85%) of enantioprobe targets identified in pairwise comparisons showed consistent stereoselective interactions in multiplexed experiments (Supplementary Datasets 1–3). Another 115 stereoselective interactions were mapped by multiplexing, and these newly discovered events mostly corresponded to proteins that were not quantified in pairwise experiments performed with the relevant enantioprobe pair(s). In addition to recapitulating and extending the stereoselective enantioprobe–protein interactions discovered in pairwise experiments, the multiplexed method also illuminated proteins that showed enrichment by one or more enantioprobe pairs, but without stereopreference. Examples included CYP27A1 and TLR8, which interacted preferentially with the (*R*)/**(*S*)-2** and (*R*)/**(*S*)-3** probe pairs, respectively, over the other enantioprobes (Fig. 5c, lower panels). We interpret these enrichment profiles to also reflect specific probe–protein interactions, where the SAR across the enantioprobe set is driven by chemotype rather than stereotype.

We reasoned that the greater sample capacity afforded by multiplexing could also provide an efficient means of assessing the

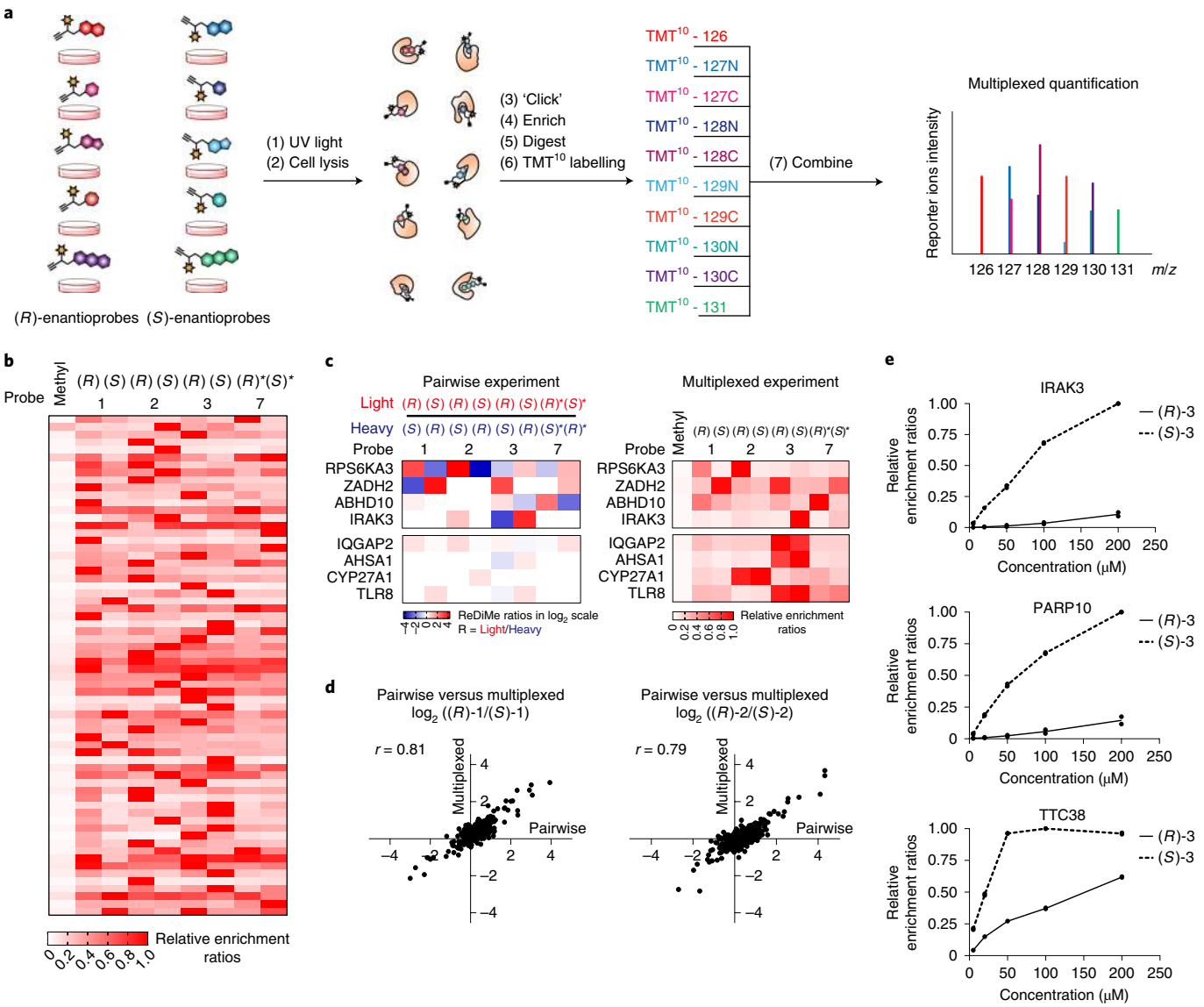

Fig. 5 | Multiplexed MS-based quantification for expedited discovery of stereoselective protein–enantioprobe interactions. a, Schematic of TMT-based workflow for mapping enantioprobe–protein interactions in a multiplex (10-plex) format. **b**, Heatmap depicting TMT quantification of stereoselective protein targets in PBMCs. Relative enrichment ratios are calculated as a percentage of maximum signal per protein. (*R*)* and (*S*)* represent (*R,R*) and (*S,S*) for enantioprobe **7**. **c**, Similar profiles are found for stereoselective protein targets of enantioprobes in pairwise (ReDiMe) versus multiplexed (TMT) experiments (top panels). Multiplexed experiments also enable the identification of proteins that interact with enantioprobes in a chemotype-selective manner (bottom panels). White signals in the heatmap correspond to either proteins with ratio values of ~1 or proteins that were not enriched and quantified with the indicated enantioprobe pair. (*R*)* and (*S*)* represent (*R,R*) and (*S,S*) for enantioprobe **7**. **d**, Representative scatter plots showing the correlation between pairwise (*x*-axis) and multiplexed (*y*-axis) experiments performed with enantioprobes (*R/S*)-**1** and (*R/S*)-**2**. Left graph contains 1,095 total quantified proteins; right graph contains 1,005 total quantified proteins. *r* values are Pearson correlation coefficients. Data reflect an average of two independently performed experiments that provided similar results (see Supplementary Dataset 2 and Supplementary Dataset 3). **e**, Concentration-dependent profiles for representative stereoselective enantioprobe–protein interactions as determined by multiplexed experiments of PBMCs treated with 0, 5, 20, 50, 100 and 200 μM of the indicated enantioprobe pair. Data reflect two independently performed experiments.

relative affinity of enantioprobe–protein interactions by comparing protein enrichment profiles across several probe concentrations. We performed a proof-of-principle experiment with a representative enantioprobe pair—(***S***)-**3** and (***R***)-**3**—tested at five different concentrations (5, 20, 50, 100 and 200 μM) in human PBMCs (Supplementary Datasets 1 and 3). The concentration-dependent profiles revealed that previously mapped enantioprobe targets maintained stereoselective interactions across the entire probe concentration range (for example, see IRAK3 and PARP10 in Fig. 5e; also see Supplementary Fig. 6). Some interactions further showed evidence of saturated enrichment at lower concentrations of the preferred enantioprobe (for example, TTC38, Fig. 5e), possibly reflecting higher affinity binding events. Consistent with this hypothesis, we found that the non-crosslinkable analogue of (***S***)-**4**, but not (***R***)-**4**, competitively blocked enantioprobe binding to TTC38 (Supplementary Fig. 6), reflecting the stereoselective enrichment profile for this protein with the (***S***)-**4** and (***R***)-**4** enantioprobe pair (Supplementary Fig. 3 and Supplementary Dataset 1).

Saturated enrichment was also observed for certain proteins that did not show stereopreference between **(*S*)-3** and **(*R*)-3** (for example, SLC25A20, Supplementary Fig. 6). Finally, a third type of profile was observed, albeit rarely, where a protein displayed saturated enrichment with both **(*S*)-3** and **(*R*)-3**, but the absolute signal plateaued at different values between the enantioprobes (for example, PTGR2, Supplementary Fig. 6). This outcome might reflect cases where equivalent binding is observed for both enantioprobes, but one of the probes generates a greater amount of photoadduct with the protein target (see Discussion below).

Taken together, these data indicate that the mapping of fragment–protein interactions in cells can be efficiently performed proteome-wide using multiplexing MS-based methods to expedite the discovery of ligandable proteins with a rich body of integrated information on potency and SAR.

Discussion

Efforts to expand the proportion of the human proteome that can be targeted by chemical probes would benefit from methods capable of evaluating small-molecule/protein interactions on a global scale in native biological systems. We previously described a chemical proteomic strategy to perform fragment-based ligand discovery experiments in human cells[13]. The initial set of FFFs uncovered many new small-molecule/protein interactions, some of which were advanced to selective and cell-active chemical probes. Nonetheless, we also found that individual FFFs showed substantially different overall protein interaction profiles in human cells, which complicated the assignment of small-molecule/protein interactions displaying authentic SARs (vs nonspecific binding to the FFFs). The enantioprobes described herein offer a general solution to this challenge by specifying ligandable proteins as those showing differential interactions with physicochemically matched compounds differing only in absolute stereochemistry. We identified many such stereoselective interactions across diverse functional and structural protein classes and verified several using recombinantly expressed proteins. In each case where a protein target had an established ligand, we found that this ligand blocked enantioprobe binding. These results indicate that stereoselective interactions of enantioprobes often occur at functional sites on proteins. If this principle generalizes across the broader set of enantioprobe targets identified herein, it highlights the potential of fragment-based screening in cells to serve as a foundation for the pursuit of chemical probes that perturb the functions of a wide range of proteins.

The broader implementation of enantioprobes for mapping protein ligandability in biological systems has important considerations. First, we emphasize that a substantial fraction of enantioprobe targets showed stereoselective interactions with only a single (*R*)/(*S*) probe pair. We interpret this result to indicate that, with our limited set of eight enantioprobe pairs, we are vastly undersampling the proportion of human proteins that have the capacity to show stereoselective interactions with small-molecule fragments. Future attention should thus be given to expanding the size and structural diversity of the enantioprobe library, as well as to applying these probes in more diverse cell types to survey a broader fraction of the human proteome. Such experiments may also uncover context-dependent enantioprobe–protein interactions, if, for instance, a protein's participation in a dynamic complex or its reversible post-translational modification state affects enantioprobe interactions. There may be further technical reasons why some stereoselective enantioprobe–protein interactions are overlooked in our chemical proteomic experiments. For instance, interactions that are too low in binding affinity may not provide sufficient enrichment of proteins for detection by MS-based proteomics, while other stereoselective interactions may be masked by multiple binding sites of a given enantioprobe on the same protein. We also admit that, in most cases, we do not know with certainty whether stereoselective interactions between an enantioprobe and a protein reflect preferential binding versus photoreactivity (that is, the extent of carbene adduct with a protein target following photoexcitation of the diazirine). In some cases, both members of an enantioprobe pair may bind equivalently to a protein target, but one probe produces a greater yield of photoadduct with the protein. While this SAR outcome would ultimately need to be clarified to guide efforts towards more advanced chemical probes that display higher affinity and selectivity for individual protein targets, we posit that stereoselective binding and stereoselective photoreactivity are equivalently useful parameters for identifying novel druggable sites in the proteome, as both would likely require specific interactions with a protein to discriminate between an enantioprobe pair. Finally, our data highlight the value of incorporating TMT-based multiplexing readouts into enantioprobe profiling experiments, which greatly expedited the discovery of stereoselective interactions without substantial losses in sensitivity or accuracy. Moreover, these multiplexing experiments provide additional SAR information by identifying proteins that interact in a chemoselective, rather than stereoselective, manner with the enantioprobe set.

Projecting forward, we envision several exciting pursuits with enantioprobes that should address fundamental questions about the ligandability of the human proteome. For instance, will the stereoselective interactions displayed by fragment enantioprobes be retained as these ligands are expanded into more advanced chemical probes, or, alternatively, will the preferential interaction with a single stereocentre dissipate in importance as additional recognition elements are built into the probes? Towards this end, the enantioprobes offer a convenient target engagement assay for assessing the competitive binding of more elaborate analogues in cells, and several of the enantiopure fragment recognition groups deployed herein are poised for direct modification using synthetic methodologies such as C–H bond activation chemistry[44–46]. Second, would more structurally complex enantioprobes identify ligandable proteins that, for instance, do not display sufficient binding affinity to simple fragment probes? Finally, what fraction of stereoselective interactions observed proteome-wide occur at functional sites on proteins? Here, we admit that a complete answer is not likely to be soon forthcoming, as we are dependent on both mapping the sites of enantioprobe binding, a still technically challenging task, and the availability of protein structures to predict functional pockets. Consider TTC38, for instance, a poorly characterized protein that has been previously identified as an off-target of the histone deacetylase inhibitor panobinostat[36] and found herein to display stereoselective interaction with the **(*S*)-4** probe that was blocked by panobinostat. We would presume that the site of binding of panobinostat and probe **(*S*)-4** is relevant to TTC38 function, but absent a structure or, for that matter, even a biochemical activity for the protein, this conclusion is premature. Of course, ligands that are found to bind silent sites on proteins can still be converted into 'functional' chemical probes that promote protein degradation using technologies of the proteolysis-targeting chimera type[47–49].

In summary, our findings demonstrate that enantioprobes offer a highly efficient way to discover small-molecule/protein interactions in human cells. Differentiating proteins based on stereoselective interactions with otherwise physicochemically equivalent fragment probes offers instant evidence of authentic ligandability. These stereoselective interactions can then form the basis for pursuit of more advanced chemical probes targeting a diverse range of proteins for basic and translational research purposes.

Methods

A detailed Methods section is provided in the Supplementary Information.

Reporting Summary. Further information on research design is available in the Nature Research Reporting Summary linked to this article.

Data availability

All data associated with this study are available in the published article and its supplementary information. The MS proteomics data have been deposited to the ProteomeXchange Consortium via the PRIDE[50] partner repository with the dataset identifier PXD015104. All other raw data are available upon request.

Received: 27 February 2019; Accepted: 10 September 2019;
Published online: 28 October 2019

References

1. Knight, Z. A. & Shokat, K. M. Chemical genetics: where genetics and pharmacology meet. *Cell* **128**, 425–430 (2007).
2. Belshaw, P. J., Ho, S. N., Crabtree, G. R. & Schreiber, S. L. Controlling protein association and subcellular localization with a synthetic ligand that induces heterodimerization of proteins. *Proc. Natl Acad. Sci. USA* **93**, 4604–4607 (1996).
3. Lai, A. C. & Crews, C. M. Induced protein degradation: an emerging drug discovery paradigm. *Nat. Rev. Drug Discov.* **16**, 101–114 (2017).
4. Lu, G. et al. The myeloma drug lenalidomide promotes the cereblon-dependent destruction of Ikaros proteins. *Science* **343**, 305–309 (2014).
5. Schreiber, S. L. A Chemical Biology View of Bioactive Small Molecules and a Binder-Based Approach to Connect Biology to Precision Medicines. *Isr. J. Chem.* **59**, 52–59 (2019).
6. Oprea, T. I. et al. Unexplored therapeutic opportunities in the human genome. *Nat. Rev. Drug Discov.* **17**, 317–332 (2018).
7. Schenone, M., Dancik, V., Wagner, B. K. & Clemons, P. A. Target identification and mechanism of action in chemical biology and drug discovery. *Nat. Chem. Biol.* **9**, 232–240 (2013).
8. Swinney, D. C. & Anthony, J. How were new medicines discovered? *Nat. Rev. Drug Discov.* **10**, 507–519 (2011).
9. Hajduk, P. J. & Greer, J. A decade of fragment-based drug design: strategic advances and lessons learned. *Nat. Rev. Drug Discov.* **6**, 211–219 (2007).
10. Bembenek, S. D., Tounge, B. A. & Reynolds, C. H. Ligand efficiency and fragment-based drug discovery. *Drug Discov. Today* **14**, 278–283 (2009).
11. Scott, D. E., Coyne, A. G., Hudson, S. A. & Abell, C. Fragment-based approaches in drug discovery and chemical biology. *Biochemistry* **51**, 4990–5003 (2012).
12. Erlanson, D. A., Fesik, S. W., Hubbard, R. E., Jahnke, W. & Jhoti, H. Twenty years on: the impact of fragments on drug discovery. *Nat. Rev. Drug Discov.* **15**, 605–619 (2016).
13. Parker, C. G. et al. Ligand and target discovery by fragment-based screening in human cells. *Cell* **168**, 527–541 e529 (2017).
14. Welsch, M. E., Snyder, S. A. & Stockwell, B. R. Privileged scaffolds for library design and drug discovery. *Curr. Opin. Chem. Biol.* **14**, 347–361 (2010).
15. Agranat, I., Caner, H. & Caldwell, J. Putting chirality to work: the strategy of chiral switches. *Nat. Rev. Drug Discov.* **1**, 753–768 (2002).
16. Nguyen, L. A., He, H. & Pham-Huy, C. Chiral drugs: an overview. *Int. J. Biomed. Sci.* **2**, 85–100 (2006).
17. Zanos, P. et al. NMDAR inhibition-independent antidepressant actions of ketamine metabolites. *Nature* **533**, 481–486 (2016).
18. Sui, J. J., Zhang, J. H., Ching, C. B. & Chen, W. N. Expanding proteomics into the analysis of chiral drugs. *Mol. Biosyst.* **5**, 603–608 (2009).
19. Sanna, M. G. et al. Enhancement of capillary leakage and restoration of lymphocyte egress by a chiral S1P1 antagonist in vivo. *Nat. Chem. Biol.* **2**, 434–441 (2006).
20. Rostovtsev, V. V., Green, L. G., Fokin, V. V. & Sharpless, K. B. A stepwise huisgen cycloaddition process: copper(I)-catalyzed regioselective "ligation" of azides and terminal alkynes. *Angew. Chem. Int. Ed. Engl.* **41**, 2596–2599 (2002).
21. Boersema, P. J., Raijmakers, R., Lemeer, S., Mohammed, S. & Heck, A. J. Multiplex peptide stable isotope dimethyl labeling for quantitative proteomics. *Nat. Protoc.* **4**, 484–494 (2009).
22. Hsu, J. L., Huang, S. Y., Chow, N. H. & Chen, S. H. Stable-isotope dimethyl labeling for quantitative proteomics. *Anal. Chem.* **75**, 6843–6852 (2003).
23. Ong, S. E. et al. Stable isotope labeling by amino acids in cell culture, SILAC, as a simple and accurate approach to expression proteomics. *Mol. Cell Proteomics* **1**, 376–386 (2002).
24. Hubbard, L. L. & Moore, B. B. IRAK-M regulation and function in host defense and immune homeostasis. *Infect. Dis. Rep.* **2**, e9 (2010).
25. Verheugd, P. et al. Regulation of NF-κB signalling by the mono-ADP-ribosyltransferase ARTD10. *Nat. Commun.* **4**, 1683 (2013).
26. Backus, K. M. et al. Proteome-wide covalent ligand discovery in native biological systems. *Nature* **534**, 570–574 (2016).
27. Bar-Peled, L. et al. Chemical proteomics identifies druggable vulnerabilities in a genetically defined cancer. *Cell* **171**, 696–709 (2017).
28. Hacker, S. M. et al. Global profiling of lysine reactivity and ligandability in the human proteome. *Nat. Chem.* **9**, 1181–1190 (2017).
29. Mitchell, L. H. et al. Novel oxindole sulfonamides and sulfamides: EPZ031686, the first orally bioavailable small molecule SMYD3 inhibitor. *ACS Med. Chem. Lett.* **7**, 134–138 (2016).
30. Van Aller, G. S. et al. Structure-based design of a novel SMYD3 inhibitor that bridges the SAM- and MEKK2-binding pockets. *Structure* **24**, 774–781 (2016).
31. Mejuch, T. et al. Small-molecule inhibition of the UNC119-cargo interaction. *Angew. Chem. Int. Ed. Engl.* **56**, 6181–6186 (2017).
32. Jaremko, L., Jaremko, M., Giller, K., Becker, S. & Zweckstetter, M. Structure of the mitochondrial translocator protein in complex with a diagnostic ligand. *Science* **343**, 1363–1366 (2014).
33. Le Fur, G. et al. Peripheral benzodiazepine binding sites: effect of PK 11195, 1-(2-chlorophenyl)-N-methyl-N-(1-methylpropyl)-3-isoquinolinecarboxamide. I. In vitro studies. *Life Sci.* **32**, 1839–1847 (1983).
34. Owen, D. R. J. & Matthews, P. M. Imaging brain microglial activation using positron emission tomography and translocator protein-specific radioligands. *Int. Rev. Neurobiol.* **101**, 19–39 (2011).
35. Rupprecht, R. et al. Translocator protein (18 kDa) (TSPO) as a therapeutic target for neurological and psychiatric disorders. *Nat. Rev. Drug Discov.* **9**, 971–988 (2010).
36. Becher, I. et al. Thermal profiling reveals phenylalanine hydroxylase as an off-target of panobinostat. *Nat. Chem. Biol.* **12**, 908–910 (2016).
37. Niphakis, M. J. et al. A global map of lipid-binding proteins and their ligandability in cells. *Cell* **161**, 1668–1680 (2015).
38. Weerapana, E., Speers, A. E. & Cravatt, B. F. Tandem orthogonal proteolysis-activity-based protein profiling (TOP-ABPP)—a general method for mapping sites of probe modification in proteomes. *Nat. Protoc.* **2**, 1414–1425 (2007).
39. Fu, W. Q. et al. Structural basis for substrate preference of SMYD3, a SET domain-containing protein lysine methyltransferase. *J. Biol. Chem.* **291**, 9173–9180 (2016).
40. Jaiswal, M. et al. Novel biochemical and structural insights into the interaction of myristoylated cargo with Unc119 protein and their release by Arl2/3. *J. Biol. Chem.* **291**, 20766–20778 (2016).
41. Thompson, A. et al. Tandem mass tags: a novel quantification strategy for comparative analysis of complex protein mixtures by MS/MS. *Anal. Chem.* **75**, 1895–1904 (2003).
42. Dayon, L. et al. Relative quantification of proteins in human cerebrospinal fluids by MS/MS using 6-plex isobaric tags. *Anal. Chem.* **80**, 2921–2931 (2008).
43. McAlister, G. C. et al. MultiNotch MS3 enables accurate, sensitive, and multiplexed detection of differential expression across cancer cell line proteomes. *Anal. Chem.* **86**, 7150–7158 (2014).
44. Ming, S. et al. Modular, Stereocontrolled Cβ–H/Cα–C Activation of Alkyl Carboxylic Acids. *Proc. Natl Acad. Sci. USA* **116**, 8721–8727 (2019).
45. Tran, A. T. & Yu, J. Q. Practical alkoxythiocarbonyl auxiliaries for iridium(I)-catalyzed C–H alkylation of azacycles. *Angew. Chem. Int. Ed. Engl.* **56**, 10530–10534 (2017).
46. Jain, P., Verma, P., Xia, G. Q. & Yu, J. Q. Enantioselective amine alpha-functionalization via palladium-catalysed C–H arylation of thioamides. *Nat. Chem.* **9**, 140–144 (2017).
47. Deshaies, R. J. Protein degradation: prime time for PROTACs. *Nat. Chem. Biol* **11**, 634–635 (2015).
48. Neklesa, T. K., Winkler, J. D. & Crews, C. M. Targeted protein degradation by PROTACs. *Pharmacol. Therapeut.* **174**, 138–144 (2017).
49. Winter, G. E. et al. Phthalimide conjugation as a strategy for in vivo target protein degradation. *Science* **348**, 1376–1381 (2015).
50. Perez-Riverol, Y. et al. The PRIDE database and related tools and resources in 2019: improving support for quantification data. *Nucleic Acids Res.* **47**, D442–D450 (2018).

Acknowledgements

We thank P. S. Baran for helpful discussions, P. X. Shen for assistance with compound characterization and R. Park for technical advice on proteomics data analysis. The authors acknowledge the Scripps Normal Blood Donor Services, NMR, MS and Automated Synthesis core facilities. J.R.R. was supported by a Postdoctoral Fellowship PF-18-217-01-CDD from the American Cancer Society. This work was supported by the National Institutes of Health (NIH) (CA231991, CA211526, GM069832 and DK114785).

Author contributions

Y.W., C.G.P. and B.F.C. conceived of the project, designed experiments and analysed data. Y.W. synthesized and characterized compounds. Y.W. performed SILAC and ReDiMe quantitative proteomics experiments and data analysis. M.M.D. developed methods for TMT labelling experiments. M.M.D. and Y.W. performed TMT-based proteomics experiments. Y.W. and J.R.R. conducted site-of-labelling experiments. Y.W. cloned and overexpressed proteins, and conducted biological experiments. H.Y.L. assisted in

biological experiments. G.B. and S.F. performed molecular modelling. Y.W. compiled proteomics data and conducted computational analyses. S.P.G., M.K., R.M.L. and G.V. assisted in the design and analysis of MS experiments. Y.W., C.G.P. and B.F.C. wrote the manuscript, and all authors contributed to manuscript editing.

Competing interests

The authors declare competing financial interests. B.F.C. is a founder and advisor to Vividion Therapeutics, a biotechnology company interested in using chemical proteomic methods to develop small-molecule drugs to treat human disease. C.G.P. serves as a consultant for Vividion Therapeutics.

Additional information

Supplementary information is available for this paper at https://doi.org/10.1038/s41557-019-0351-5.

Correspondence and requests for materials should be addressed to C.G.P. or B.F.C.

nature research

Corresponding author(s): Christopher G. Parker, Benjamin F. Cravatt

Last updated by author(s): Aug 21, 2019

Reporting Summary

Nature Research wishes to improve the reproducibility of the work that we publish. This form provides structure for consistency and transparency in reporting. For further information on Nature Research policies, see Authors & Referees and the Editorial Policy Checklist.

Statistics

For all statistical analyses, confirm that the following items are present in the figure legend, table legend, main text, or Methods section.

n/a	Confirmed	
☐	☒	The exact sample size (*n*) for each experimental group/condition, given as a discrete number and unit of measurement
☐	☒	A statement on whether measurements were taken from distinct samples or whether the same sample was measured repeatedly
☐	☒	The statistical test(s) used AND whether they are one- or two-sided *Only common tests should be described solely by name; describe more complex techniques in the Methods section.*
☒	☐	A description of all covariates tested
☒	☐	A description of any assumptions or corrections, such as tests of normality and adjustment for multiple comparisons
☐	☒	A full description of the statistical parameters including central tendency (e.g. means) or other basic estimates (e.g. regression coefficient) AND variation (e.g. standard deviation) or associated estimates of uncertainty (e.g. confidence intervals)
☒	☐	For null hypothesis testing, the test statistic (e.g. *F*, *t*, *r*) with confidence intervals, effect sizes, degrees of freedom and *P* value noted *Give P values as exact values whenever suitable.*
☒	☐	For Bayesian analysis, information on the choice of priors and Markov chain Monte Carlo settings
☒	☐	For hierarchical and complex designs, identification of the appropriate level for tests and full reporting of outcomes
☐	☒	Estimates of effect sizes (e.g. Cohen's *d*, Pearson's *r*), indicating how they were calculated

Our web collection on statistics for biologists contains articles on many of the points above.

Software and code

Policy information about availability of computer code

Data collection	Xcalibur v2.2 was used for mass spectrometry data collection. Image Lab v5.2.1 was used for fluorescence gel scanning. CLARIOstar v5.4 was used for absorbance (Pierce BCA Protein Assay) data collection. Li-COR Odyssey v3.0.30 was used for IRDye secondary antibodies imaging.
Data analysis	RAWconverter (v1.1.0.22) was used to convert raw mass spectrometry files to .ms2 and .mzXML files. Integrated Proteomics Pipeline (IP2) v6.0.02, DTASelect 2.0 (embedded in IP2) and in-house software CIMAGE (Weerapana, E. et al. 2010) were used to analyze all mass spectrometry data, including SILAC-, ReDiMe- and TMT-based experiments. RStudio (v1.1.456, R version 3.5.1) was used to compile proteomics data. Image Lab v5.2.1 was used for relative quantization of fluorescence gel scanning. Image Studio Lite v5.2.5 was used to process western blot images. GraphPad Prism v7.03 was used to perform statistical tests and to generate all graphs and plots. AutoDock v4.2.6 and AutoDockTools were used for molecular modeling.

For manuscripts utilizing custom algorithms or software that are central to the research but not yet described in published literature, software must be made available to editors/reviewers. We strongly encourage code deposition in a community repository (e.g. GitHub). See the Nature Research guidelines for submitting code & software for further information.

Data

Policy information about availability of data

All manuscripts must include a data availability statement. This statement should provide the following information, where applicable:

- Accession codes, unique identifiers, or web links for publicly available datasets
- A list of figures that have associated raw data
- A description of any restrictions on data availability

All data associated with this study are available in the published article and its supplementary information. The mass spectrometry proteomics data have been deposited to the ProteomeXchange Consortium via the PRIDE partner repository with the dataset identifier PXD015104. All other raw data are available upon request.

Field-specific reporting

Please select the one below that is the best fit for your research. If you are not sure, read the appropriate sections before making your selection.

☒ Life sciences ☐ Behavioural & social sciences ☐ Ecological, evolutionary & environmental sciences

For a reference copy of the document with all sections, see nature.com/documents/nr-reporting-summary-flat.pdf

Life sciences study design

All studies must disclose on these points even when the disclosure is negative.

Sample size	No statistical methods were used to pre-determine the sample size. Sample size (N ≥ 2) was chosen according to literature showing similar methods of analysis.
Data exclusions	No data was excluded
Replication	All experiments were performed at least twice independently at different time points. Similar results were obtained after data analysis in all attempts. Therefore all attempts at replication were successful.
Randomization	Cell lines used in experiments were grown under identical conditions, and therefore randomization was not used. Human blood was acquired from de-identified healthy patient donors. No experimental human groups were designated in this study, therefore randomization was not used.
Blinding	Cell lines used in experiments were grown under identical conditions, human blood was acquired from de-identified healthy patient donors (female and male, age 30-65), and therefore blinding was not used.

Reporting for specific materials, systems and methods

We require information from authors about some types of materials, experimental systems and methods used in many studies. Here, indicate whether each material, system or method listed is relevant to your study. If you are not sure if a list item applies to your research, read the appropriate section before selecting a response.

Materials & experimental systems

n/a	Involved in the study
☐	☒ Antibodies
☐	☒ Eukaryotic cell lines
☒	☐ Palaeontology
☒	☐ Animals and other organisms
☐	☒ Human research participants
☒	☐ Clinical data

Methods

n/a	Involved in the study
☒	☐ ChIP-seq
☒	☐ Flow cytometry
☒	☐ MRI-based neuroimaging

Antibodies

Antibodies used	Primary: Mouse anti-FLAG® clone M2 (Sigma Aldrich, SKU F1804-1MG, 1:10000 dilution). Secondary: IRDye® 800CW Goat anti-Mouse secondary antibody (LICOR, 925-32210, 1:10000 dilution).
Validation	Mouse anti-FLAG® clone M2 (Sigma Aldrich, SKU F1804-1MG): validated for western blotting by manufacturer using extracts from CHO cells with spiked FLAG-BAP protein.

Eukaryotic cell lines

Policy information about cell lines

Cell line source(s)	HEK293T (ATCC)
Authentication	All cell lines used in this study were authenticated by the vendors
Mycoplasma contamination	All cell lines used in this study were tested negative for mycoplasma
Commonly misidentified lines (See ICLAC register)	No commonly misidentified cell lines were used in this study

Human research participants

Policy information about studies involving human research participants

Population characteristics	Healthy donors were recruited through Scripps Research's Normal Blood Donor Services (NBDS), which has the following requirements: Be between 30 and 65 years of age. Weigh at least 110 pounds (50 kg). Have a Body Mass Index (BMI) between 19 – 39. Have blood pressure between 90-180 mm Hg systolic and 50-100 mm Hg diastolic. Not have had major surgery within the past six months. Have had an adequate hemoglobin on initial screening test. Have negative screening for HIV and Hepatitis B, C, at initial screening, and annually thereafter. Is not on daily aspirin or daily anti-inflammatory medications. No auto-immune diseases.
Recruitment	Healthy donors were recruited through Scripps Research's Normal Blood Donor Services (NBDS) after informed consent. All donors are initially screened for infectious diseases prior to being recruited, and screened on a yearly basis after the initial screen to remain active in the program. Human blood is acquired on a as needed basis. No self-selection of donors is involved.
Ethics oversight	The Scripps Research Institute Institutional Review Board.

Note that full information on the approval of the study protocol must also be provided in the manuscript.